THE ASTROPHYSICAL JOURNAL, 558:165–175, 2001 September 1

THE PHYSICAL BASIS FOR THE SILICATE DUST SEQUENCE

M. P. EGAN[1] AND G. C. SLOAN[2]

Received 2000 October 6; accepted 2001 May 2

ABSTRACT

Using a series of radiative transfer models of circumstellar dust shells, we explore the physical origins of the variety of shapes of the 10 μm silicate feature seen in the spectra of oxygen-rich circumstellar dust shells. In order to match the full range of observed spectral shapes, the models explore four parameters: the relative abundance of amorphous alumina and amorphous silicates, the inner dust shell radius, the optical depth, and the geometric thickness of the shell. Optically thin shells dominated by amorphous silicate grains reproduce the classic narrow silicate feature at 10 μm. Increasing the optical depth of the shell produces spectral features at 10 μm with stronger components at 11 μm, but to match the [12]−[25] *IRAS* colors, these optically thick shells must be geometrically thin (i.e., have a truncated outer radius). Spectra with broad, low-contrast emission features peaking at wavelengths longer than $\sim$11 μm originate from optically thin shells composed of amorphous alumina. These findings provide a physical basis for the silicate dust sequence defined by Sloan & Price. We suggest that the [12]−[25] color is an indicator of geometric shell thickness. Thin shells can only arise if the star ejects mass and forms dust in a noncontinuous process.

Subject headings: circumstellar matter — dust, extinction — infrared: stars

1. INTRODUCTION

Over half of the sample of 5400 mid-infrared spectra obtained by the Low-Resolution Spectrometer (LRS) aboard the *Infrared Astronomical Satellite* (*IRAS*) arise from optically thin circumstellar dust shells composed of oxygen-rich dust. Early classification efforts analyzed these oxygen-rich dust spectra based on the relative strength of the classic silicate feature at 10 μm compared to the stellar photosphere (e.g., *IRAS* Science Team 1986).

Little-Marenin and collaborators introduced a different approach by concentrating on the shape of the dust spectrum and ignoring the contrast between the dust and the star (Little-Marenin & Price 1986; Little-Marenin & Little 1988, 1990, hereafter referred to collectively as LML). They assumed that the total spectrum could be approximated as a sum of spectra from the stellar photosphere and the circumstellar dust shell. By fitting the stellar contribution at $\sim$8 μm and subtracting it, they isolated the contribution from the dust. This step avoided any confusion caused by differences in the relative strength of the dust spectrum from one star to the next. It revealed that oxygen-rich dust shells produced spectra that could be classified into several groups depending on the relative strengths of the strong silicate feature at 10 μm, secondary features at 11 and 13 μm, and broad, low-contrast emission in the 12–13 μm region.

Sloan & Price (1995, 1998, hereafter referred to collectively as SP) modified the LML classification by using the ratios of the flux from the dust shell at 10, 11, and 12 μm to quantify the shape of the dust feature. Using the flux ratios (or colors) F_{10}/F_{11} and F_{10}/F_{12}, they showed that all of the LML classes for oxygen-rich dust spectra fell along one smooth spectral progression, which they called the *silicate dust sequence*.

To classify spectra, SP divide the silicate dust sequence into eight segments (Fig. 1). Classic silicate dust spectra, characterized by a narrow emission band centered near 10 μm, produce the highest values of F_{10} compared to F_{11} or F_{12}. The SP system declares these SE8, and as Figure 1 shows, they reside on the upper part of the silicate dust sequence [SE: silicate emission]. As the relative contribution from an additional spectral component at 11 μm increases, these spectra shift down the silicate dust sequence through SE7 to SE3. At the bottom end of the silicate dust sequence, SE1–SE2, the emission feature is broad and peaked longward of 11 μm so that F_{10}/F_{11} and F_{10}/F_{12} are at a minimum. Sloan & Price (1998) divide these classes into three groups: classic silicate emission (SE7–SE8), structured silicate emission (SE3–SE6), and broad dust emission (SE1–SE2). Table 1 summarizes the properties of these groups, and Figure 2 shows a sample spectrum from each.

Spectra from each SE index show a wide range of contrasts between dust emission and stellar photosphere (Sloan & Price 1995; see their Fig. 4). While the contrast does grow with increasing SE index, the overlap in contrast between indices is substantial. As Figure 3 illustrates, the [12]−[25] color from the *IRAS* 12 and 25 μm bands behaves similarly. It generally reddens with increasing SE index, but the change from one index to the next is small compared to the range of colors within each index. Thus, neither contrast nor color can effectively distinguish the SE index, which quantifies the shape of the spectral emission from the dust.

While the silicate dust sequence has provided a means of ordering the rich variation seen in oxygen-rich dust spectra, the physical origins of the sequence remain unclear. Emission spectra from oxygen-rich dust can be approximated with the equation

$$S_{\rm dust}(\lambda) = \sum_i B(\lambda, T_i) Q_i(\lambda)(1 - e^{-\tau_i(\lambda)}) , \qquad (1)$$

where the summation is over each component of the dust shell. This equation contains three variables: temperature, optical depth, and optical efficiencies of the dust, which

[1] Air Force Research Laboratory, Space Vehicles Directorate, 29 Randolph Road, Hanscom AFB, MA 01731-3010.
[2] Institute for Scientific Research, Boston College, 140 Commonwealth Avenue, Chestnut Hill, MA 02467-3862.

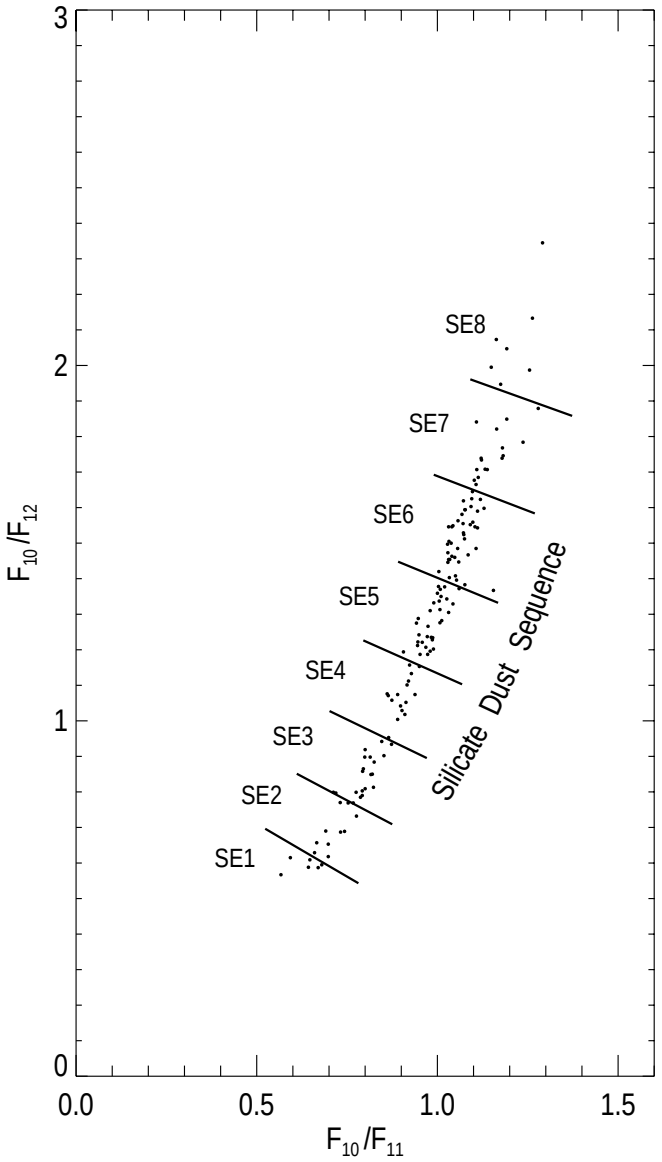

FIG. 1.—Flux ratios from the dust obtained after subtracting an estimated stellar contribution for the brightest sources in the AGB sample from Sloan & Price (1998). These data define the silicate dust sequence.

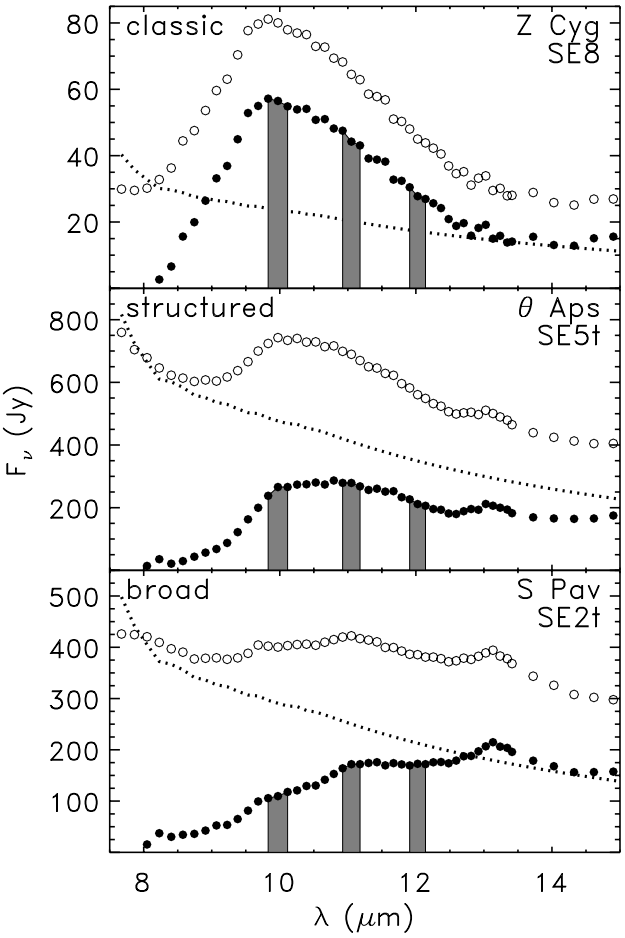

FIG. 2.—Sample spectra for classic silicate emission (*top*), structured silicate emission (*middle*), and broad oxygen-rich dust emission (*bottom*). In each panel, the open circles trace the total spectrum (star plus dust), the dashed line shows the fitted stellar continuum, and the filled circles trace the dust emission after subtracting the stellar continuum. The shaded vertical bars mark the wavelengths used to determine the flux ratios F_{10}/F_{12} and F_{11}/F_{12}.

depend primarily on the chemical composition of the dust grains. For each chemical component in the shell, the summation will be over a range of distances from the central star, so actually four variables contribute to the final spectrum: (1) temperature distribution, (2) optical depth, (3) geometric thickness, and (4) chemical composition.

The silicate dust sequence must result from changes in one or more of these variables, and most have been proposed as the explanation. Vardya, de Jong, & Willems (1986) and Little-Marenin & Price (1986) suggested a chemical dependence, with silicates producing the classic emission feature and alumina material producing the broad emission feature (Onaka, de Jong, & Willems 1989). Ivezić & Elitzur (1995, hereafter IE95) argued that by varying only the optical depth, they can match the LML emission classes equivalent to the classes SE3–SE8. Variations in the temperature of the dust shell have also been suggested (Hron, Aringer, & Kerschbaum 1997).

To test these possibilities, we have produced a series of radiative transfer models that explore a range of parameters. We consider two dust materials: amorphous silicates, which clearly produce the classic spectral features seen on the upper silicate dust sequence, and amorphous alumina, which may be responsible for the broad emission features produced on the lower silicate dust sequence. The goal is to

TABLE 1

PROPERTIES OF THE OXYGEN-RICH DUST EMISSION CLASSES

Class Description	SE Index	Location On Silicate Dust Sequence	Sample Spectrum
Classic silicate emission	SE7–SE8	Upper	Fig. 2 (*top*)
Structured silicate emission	SE3–SE6	Central	Fig. 2 (*middle*)
Broad O-rich dust emission.....	SE1–SE2	Lower	Fig. 2 (*bottom*)

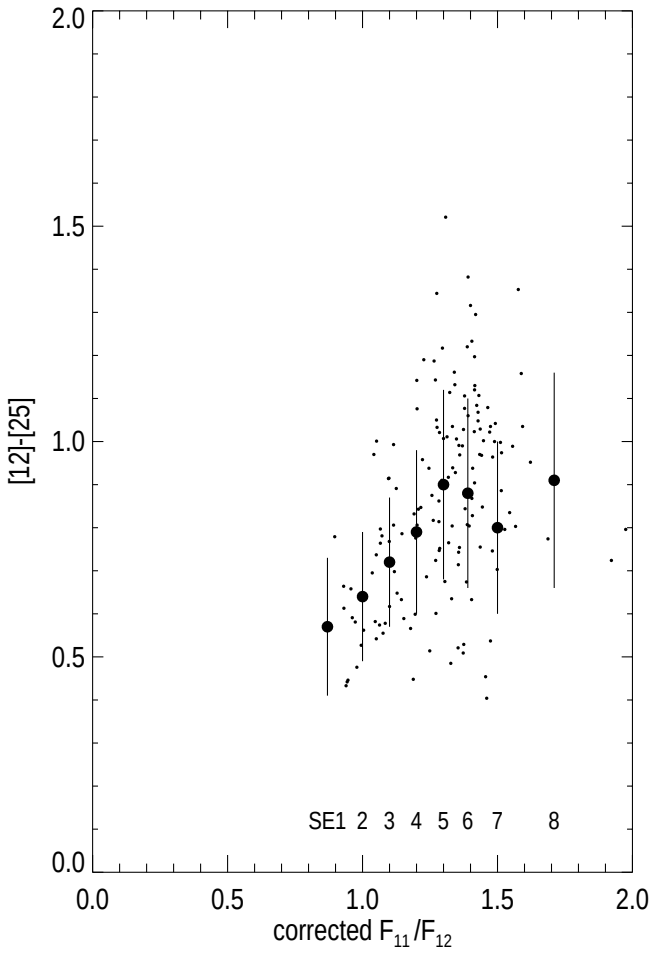

FIG. 3.—*IRAS* [12]−[25] colors as a function of location on the silicate dust sequence for the brightest AGB sources from Sloan & Price (1995). The corrected flux ratio F_{11}/F_{12} is determined using the method of Sloan & Price. Small filled circles represent the individual sources, while large filled circles with error bars show the mean color and standard deviation for each silicate emission index.

determine if combinations of these two grain compositions can produce each of the eight SE indices along the silicate dust sequence and, if so, what other physical properties the dust shell must have.

We analyze the radiative transfer models using the methods of SP. To fit a particular SE index, the dust spectrum from the model must produce flux ratios (F_{10}/F_{11} and F_{10}/F_{12}) that are consistent with the observed silicate dust sequence (Fig. 1). In addition, the total spectrum must have an appropriate [12]−[25] color (Fig. 3). Section 2 describes the models, § 3 presents the results, and in § 4, we discuss what the silicate dust sequence can actually reveal about the dust shells it classifies.

2. MODELS

We model spectra from oxygen-rich circumstellar shells using the radiative transfer code described by Egan, Leung, & Spagna (1988), which is based on the quasi-diffusion method of Leung (1976). All models assume a star embedded within a single spherically symmetric dust shell. Inputs to the model are the stellar temperature T_* and luminosity L_* (the stellar radius R_* is computed from T_* and L_*), the inner radius of the dust shell R_{in}, the geometric thickness of the dust shell ΔR (the difference in radii between the inner and outer edges of the shell), the total opacity of the dust shell at 10 μm (τ_{10}) , the dust density distribution $n(r)$, the extinction properties of the dust $Q_{abs}(\lambda)\pi a^2$ and $Q_{sca}(\lambda)\pi a^2$, and the scattering asymmetry parameter $\langle g(\lambda)\rangle$. The code solves the radiative transfer problem, determines the temperature distribution in the dust shell, and produces the spectral energy distribution (SED) of the observed flux.

2.1. *Assumptions of the Model*

While the radiative transfer code requires that seven input parameters be specified, three of these can be fixed without affecting the answers to the questions we are asking about the silicate dust sequence.

First, all models use $L_* = 10^4\ L_\odot$. Ivezić & Elitzur (1997) show that luminosity only acts as a scaling factor for the emission and does not affect the spectral shape. Thus, the quantities we are interested in, flux ratios, spectral shape, and infrared colors, do not depend on L_*.

Second, the stellar temperature $T_* = 2500$ K for all models. The stellar temperature and luminosity will determine where the dust forms and at what initial number density (Egan & Leung 1995), but these parameters are included explicitly in the radiative transfer code (as R_{in} and τ_{10}). Regardless of T_*, gas still condenses into dust at its characteristic condensation temperature. Changing T_* will shift the location of the condensation radius with respect to the specified R_{in}. This would change the temperature of the dust at R_{in} and through the shell, which would effect the emergent spectrum. However, a shift in R_{in} could compensate completely for a shift in T_*. There is no need to vary both parameters in our models.

Finally, the dust density distribution follows an inverse square law: $n(r) = n_0(R_{in}/r)^2$, a direct result of a steady spherical outflow. Questions about the applicability of this assumption to envelopes of stars on the asymptotic giant branch (AGB) have been raised (see IE95 and references within). Whatever the actual form of the distribution law, the processes driving the mass outflow are likely to be the same for all of the silicate emission sources and produce similar, if not identical, dust density distributions, making any explorations of variations in density distributions unproductive. The above assumptions are consistent with previous results (Chan & Kwok 1990; Egan et al. 1996; Ivezić & Elitzur 1997), which show that for a given dust density distribution, the opacity, the inner and outer radii of the dust shell, and the dust composition determine the spectral shape.

2.2. *The Model Grid*

This study uses three sets of models, each in turn improving on the previous set. The objective is to find a set of parameters that matches the spectral emission from each of the eight SE indices.

For the dust extinction properties, we computed absorption and scattering cross sections and scattering coefficients from Mie theory, assuming that all the grains were spheres of radius 0.03 μm. Grain size and shape do not vary in these models because these parameters have only a slight effect on the shape of the 10 μm silicate emission feature, which is much smaller than the changes in shape modeled here. Indeed, even such extremes as comparing fractal grains to spherical grains result in little change in the shape of the 10

μm feature (as defined by the SP method; see Fogel & Leung 1998).

The grid examines two different grain types: amorphous silicates and amorphous alumina. Silicates are represented by optical constants from Ossenkopf, Henning, & Mathis (1992); they derive these from LRS observations of circumstellar shells. Alumina grains are represented by the optical constants of Koike (1995; we use the constants for the more disordered material, rocket exhaust).

In the first model set, we vary the chemical composition of the dust, the inner radius of the shell, and the total opacity of the shell but keep the geometric thickness of the shell fixed. In the second model set, we fix the inner dust shell radius, reduce the chemical compositions and opacities to those compatible with the data, and focus on the effects of varying the geometric thickness of the shell. In the third set we refine the parameters to produce spectra for each SE index similar to the LRS data.

2.3. *Analysis of Spectral Energy Distributions*

Each model produces a complete SED from 0.36 to 1000 μm. Convolving the emergent flux with the *IRAS* bandpasses (Beichman et al. 1986) determines the *IRAS* colors of the model (see the Appendix for the definition of *IRAS* magnitudes and colors). To classify a spectrum, we follow the procedure outlined by SP, with one exception. Since the input spectrum is a 2500 K blackbody, we fit and remove this spectrum and not a more complicated combination of an Engelke (1992) function and SiO absorption (which would be more appropriate to sources observed by the LRS). The classification is based on the relative fluxes from the dust at 10, 11, and 12 μm.

To match the silicate dust sequence, a model must reproduce the flux ratios F_{10}/F_{11} and F_{10}/F_{12}. In other words, in plots similar to Figure 1, the models must fall along the silicate dust sequence. The models must also fall within the range of *IRAS* [12]$-$[25] colors appropriate to their location on the silicate dust sequence (Fig. 3).

3. RESULTS

3.1. *Model Set 1*

The first model set examines the effects of dust grain composition, opacity, and the inner dust shell radius over a wide range of values. For all these models, we fix the geometric thickness of the shell $\Delta R = R_{\rm out} - R_{\rm in}$ at 10^{17} cm. For dust grain composition, we use 11 different mixtures, all of aluminum oxide and amorphous silicates, ranging from 100% (by number) alumina grains to 100% silicate grains in 10% increments. While expressing the composition as a percentage of grain type by number density is convenient for modeling purposes, it is not useful astrophysically since the opacity due to a dust type depends on its number density and its extinction cross section, and these are size-dependent. The astrophysically relevant quantity is the percent of opacity due to each grain type. Table 2 gives the conversion between grain abundance (as a percent by number) and the fraction of total opacity (at 10 μm) due to each grain component for model set 1.

For each composition, the models have six different opacities at 10 μm ($\tau_{10} = 0.01$, 0.03, 0.1, 0.3, 1.0, and 3.0), and for each opacity, the models have five inner dust shell radii (2, 3, 5, 7, and $10R_*$). These values of $R_{\rm in}$ translate into maximum dust temperatures $T_{\rm in}$ between $\sim$2400 and $\sim$800 K. Thus, model set 1 represents a three-dimensional grid of 330 models.

TABLE 2

GRAIN ABUNDANCE BY NUMBER DENSITY VERSUS CONTRIBUTION TO DUST OPACITY

Silicate (% by number)	Silicate τ_{10} (%)	Al_2O_3 (% by number)	Al_2O_3 τ_{10} (%)
0	0	100	100
5	12	95	88
10	22	90	78
20	39	80	61
30	52	70	48
40	63	60	37
50	72	50	28
60	79	40	21
70	86	30	14
80	91	20	9
90	96	10	4
95	98	5	2
100	100	0	0

Figure 4 compares the flux ratios produced by the models to LRS data, and it illustrates the following important points:

1. Compositions with a minority dust component of 20% or more do not produce flux ratios that fall on the silicate dust sequence. These models are plotted with open symbols in Figures 4 and 5 to indicate that they fail to match the observed data. In other words, the shell must be dominated by either alumina or silicate dust. Relatively even mixtures of the two do not work.
2. The lower silicate dust sequence, populated by spectra with broad, low-contrast emission features, originates from optically thin shells of alumina dust ($\tau_{10} \lesssim 3.0$). The pure alumina shells line up with the SE1–SE2 range of the sequence better than shells with 10% silicates.
3. The upper silicate dust sequence, populated by sources with a strong and narrow silicate feature (the classic silicate feature), originates from optically thin shells of relatively pure amorphous silicates ($\tau_{10} \lesssim 1.0$). The models with 90% silicates run along the lower edge of the upper sequence and do not fit the data as well as more pure silicate shells.
4. Increasing either the optical depth or the inner radius of the shell moves a model from one end of the silicate dust sequence toward the center. For silicate shells, increasing either parameter produces cooler dust, which leads to increased self-absorption of the emission feature at 10 μm, broadening the feature and driving the flux ratios down the silicate dust sequence. Thus, optically thin shells of amorphous silicates successfully reproduce the upper silicate dust sequence, and increasing either the opacity or inner radius of the shell fits *nearly the entire silicate dust sequence.*

Figure 5 compares the *IRAS* [12]$-$[25] color of the models with observed data. All of the silicate models not already ruled out by Figure 4 lie in a narrow band. With the geometric shell thickness fixed (at $\Delta R = 10^{17}$ cm), increasing the optical depth of a silicate shell will shift the dust emission to lower values of F_{11}/F_{12} (i.e., down the silicate dust sequence), but it also reddens the [12]$-$[25] color of the total spectrum. The colors of observed sources, on the other hand, grow more blue toward lower flux ratios. Con-

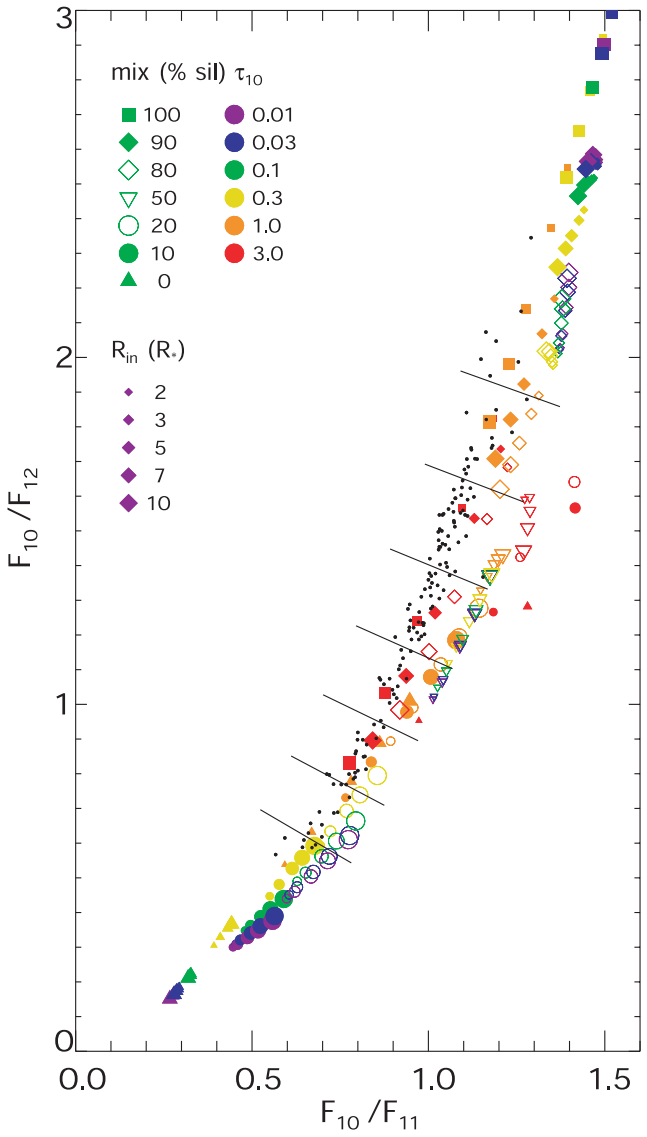

FIG. 4.—Flux ratios at 10, 11, and 12 μm for model set 1, compared to observed data. Different symbols represent differing amounts of alumina and silicate dust. Colors range from violet for optically thin shells to red for optically thick shells, and the size of the symbols scales with the inner radius of the dust shell. The small filled circles are observed data, as in Fig. 1. The open symbols mark dust mixtures that do not produce dust spectra on the silicate dust sequence. Only mixtures with more than 80% silicates or 80% alumina match the actual data, with alumina shells reproducing the lower silicate dust sequence and silicate shells reproducing the upper sequence. Increasing either inner radius or optical depth of the shell drives the models from the ends of the sequence toward the center.

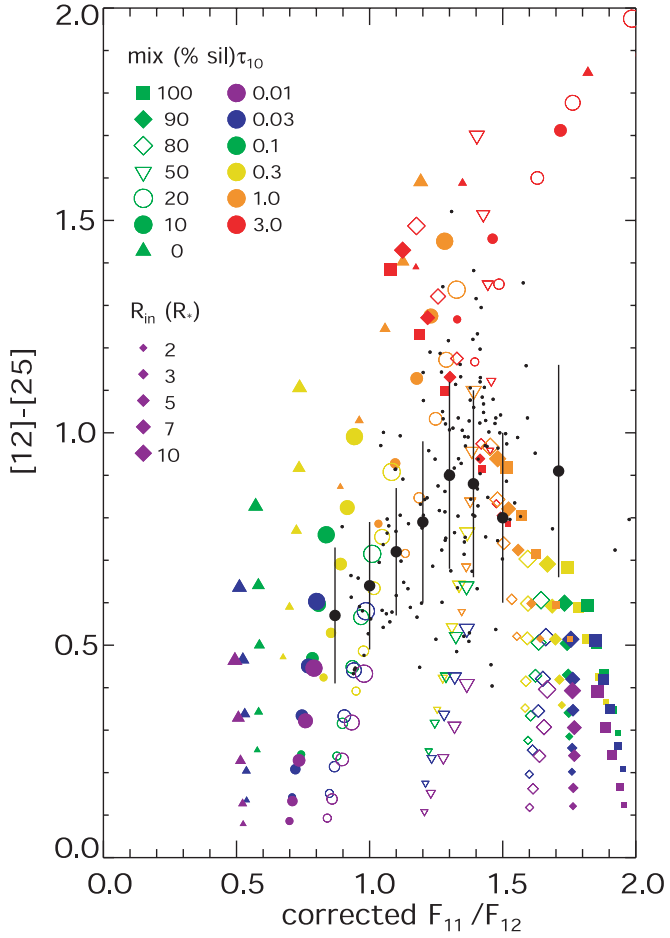

FIG. 5.—*IRAS* [12]−[25] color as a function of location along the silicate dust sequence for model set 1. Symbols and colors are as defined for Fig. 4. The only models with [12]−[25] colors near the mean color for SE3, SE4, and SE5 are plotted with open symbols, which means that they have been ruled out in Fig. 4.

sequently, these silicate models cannot fit SE indices below SE5. Even at SE5, the model colors are nearly a full standard deviation redder than the mean.

In the SE3–SE5 range, the models that best fit the [12]−[25] colors are the more even mixtures, which Figure 4 has already ruled out.

In the SE1–SE2 range, pure alumina models are too red, and while models with 10% silicates can match the SE1 data quite well, they also are too red for most of the SE2 sources.

The SE8 region also presents difficulties. Model shells with enough warm dust to fit the flux ratios are too blue to fit the [12]−[25] colors of most of the observed sources. We have not found any combination of parameters that can fit the redder [12]−[25] colors without slipping down the silicate dust sequence to indices lower than SE8.

To summarize the results of model set 1, the extreme ends of the silicate dust sequence are composed of the dust shells with the lowest opacity, with alumina dust producing broad emission features and amorphous silicates producing classic silicate features. Shells with cooler dust temperatures (as a result of either higher optical depth or larger inner shell radius) can reproduce only some of the structured silicate features in the middle of the sequence.

3.2. *Model Set 2*

Model set 1 produces flux ratios that fit the silicate dust sequence, but the [12]−[25] colors are too red to fit structured silicate sources (SE3–SE5), implying that the models contain too much cool dust. To reduce the amount of cool dust, model set 2 explores the effect of varying the geometric thickness of the shell, which in model set 1 remained fixed at $\Delta R = 10^{17}$ cm. In addition, the inner radius of the dust shell is now fixed at $R_{in} = 3R_*$ (corresponding to a condensation temperature of $\sim$2000 K). This limits the models to cases of ongoing mass loss (or undetached shells), and it allows a comparison of the effects of variations of geometric thickness with variations of R_{in} in model set 1.

The geometric thickness varies over the increments $\Delta R = 3.0 \times 10^{15}$, 3.0×10^{16}, 3.0×10^{17}, and 3.0×10^{18} cm, and the compositions are now limited to pure silicates and pure alumina.

Figure 6 shows that varying the geometric thickness of the shell does not affect the flux ratios significantly. The largest shifts are approximately one SE index. In general, the flux ratios are much less sensitive to variations in geometric thickness than they are to variations in the inner dust shell radius.

Figure 7 shows that changes in the geometric thickness of the shell have a more substantial effect on the [12]−[25] color, but only for models with $\Delta R < 3 \times 10^{16}$ cm.[3] Geometrically thinner shells correspond to significantly bluer infrared colors. This degree of freedom makes it possible to use *optically thick but geometrically thin* shells of amorphous silicates to explain both the flux ratios and the [12]−[25] colors of structured silicate sources (SE3–SE7), although we need to expand our parameter space to geometrically thinner shells to match the observed data for the lower silicate dust sequence. Since the maximum [12]−[25] color results from a thinner geometric thickness than used in model set 1, we cannot use this degree of freedom to improve the fit to the redder SE8 sources since we can only make the [12]−[25] color more blue.

[3] At this limit, a dust grain traveling 10 km s^{-1} would take 1000 yr to move from the inner radius of the shell to the outer edge. Shell structures beyond this limit (i.e., mass loss originating >1000 yr ago) would influence colors at longer wavelengths (e.g., [25]−[60]). We use the term "geometrically thin" to describe shells with $\Delta R < 3 \times 10^{16}$ cm.

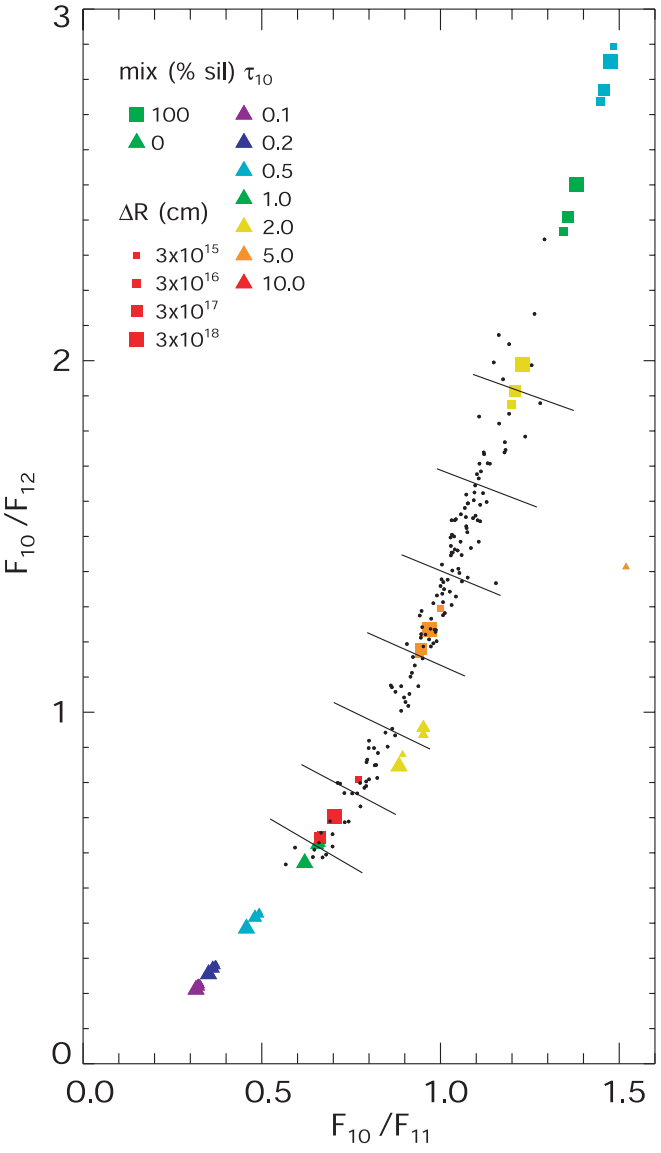

FIG. 6.—Flux ratios for model set 2. The symbols are defined as in Fig. 4, except that here the size of the symbol indicates the geometric thickness of the dust shell. All models fall on the silicate dust sequence.

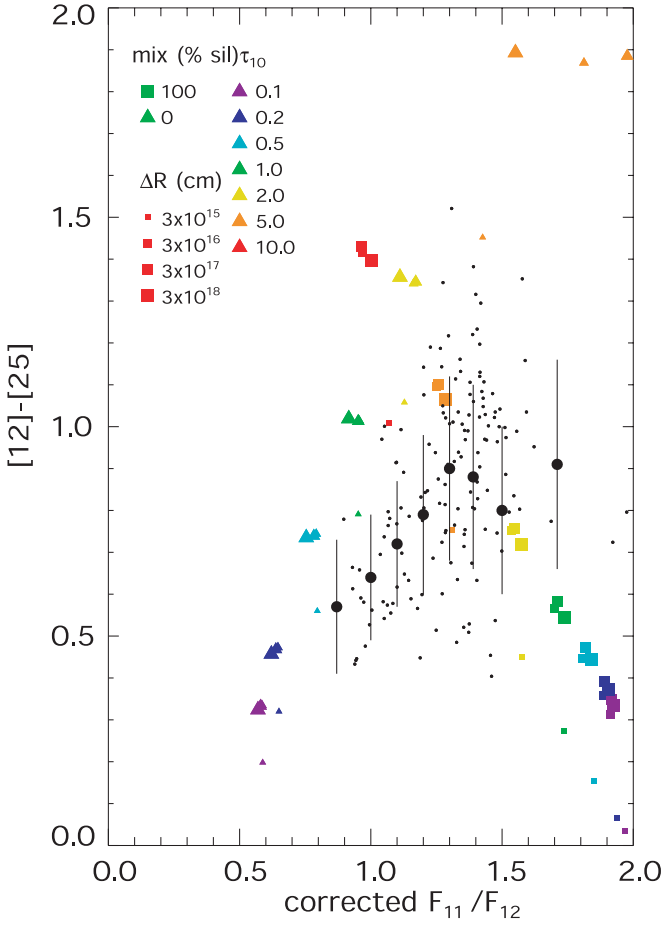

FIG. 7.—Infrared colors for model set 2, using symbols as defined for Fig. 6. The geometrically thinnest shells reduce the discrepancy in [12]−[25] color for the optically thicker models.

3.3. *Model Set 3*

Model sets 1 and 2 demonstrate that variations in chemical composition, dust temperature (which depends primarily on inner dust shell radius and, to a lesser degree, on optical thickness), and geometric thickness can reproduce *both* the narrowband flux ratios *and* broadband infrared colors of the entire silicate dust sequence. Model set 3 refines the parameter grid with the goal of actually matching the full spectral properties of the dust emission from each of the eight SE indices.

We use the two compositions from model set 2 (pure silicate and pure alumina) and focus on values of shell thickness and opacity that will span the observed data. For ΔR, these range from 6×10^{14} to 3×10^{16} cm. For silicate

models, τ_{10} runs from 2.0 to 10.0, while for alumina models, τ_{10} ranges between 0.4 and 1.5.

Figure 8 demonstrates that model set 3 provides good matches to the flux ratios of the complete silicate dust sequence. Figure 9 shows that these models fit nearly the full range of [12]−[25] colors over the silicate dust sequence, except for SE8 (as before) and the reddest SE5–SE7 sources.

Using Figure 9 as a guide, we attempt to fit the mean spectrum from each SE index by iterating τ_{10} and ΔR until a model reproduces both the mean corrected flux ratio F_{11}/F_{12} and the mean [12]−[25] color for that index. This method avoids the problem of fitting spectra from individual sources, with their troublesome idiosyncrasies. We used alumina models for SE1–SE3 and silicate models for SE3–SE7. Table 3 provides the parameters that fit the observed data best.

Figure 10 compares the synthetic spectra from our best-fit models with actual LRS data. Fitting the detailed spectrum was not a constraint for our model, but it is interesting to compare them. The synthetic spectra from the optically thin alumina shells match the actual SE1 and SE2 spectra remarkably well. Similarly, optically thin silicate shells match the classic silicate features on the upper silicate dust sequence well (recall that Ossenkopf et al. 1992 determined their optical constants to do just this).

The perhaps unexpected result is that the apparent shoulder at 11 μm, which grows relative to the 10 μm feature from SE7 to SE3, results simply from increasing the optical depth of the shell. This drives the silicate emission feature into self-absorption, decreasing the contribution at 10 μm.

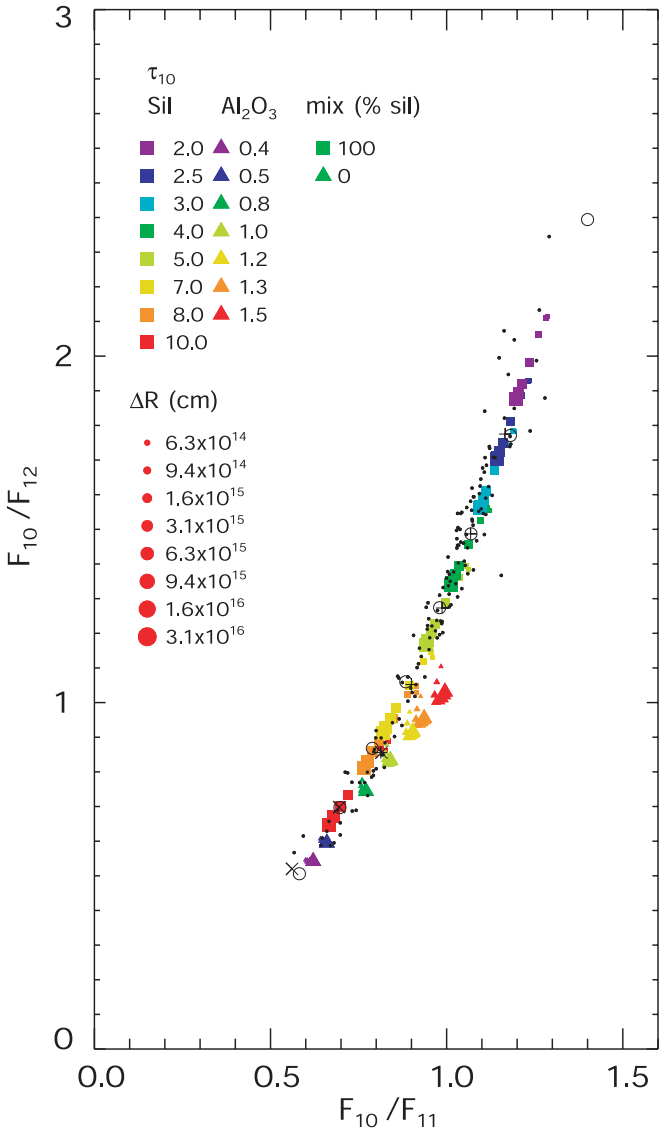

FIG. 8.—Flux ratios for model set 3. The symbols are defined similarly in Fig. 6. Varying the opacity and geometric shell thickness for pure alumina and pure silicate shells reproduces the full silicate dust sequence.

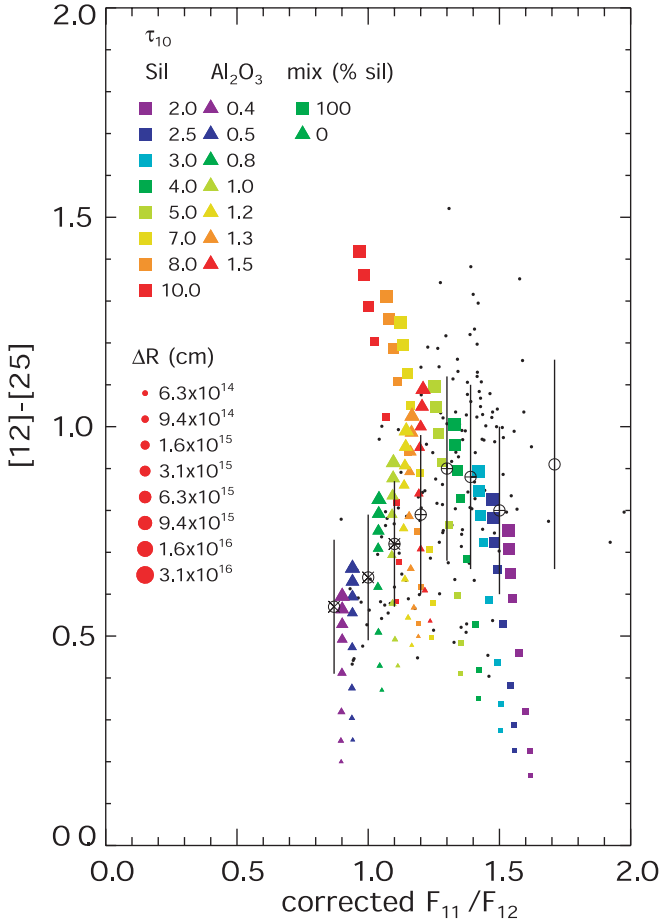

FIG. 9.—Infrared colors for model set 3, using symbols as defined for Fig. 8. The parameters used can account for nearly all colors at all SE indices.

TABLE 3

PARAMETERS OF THE MODELS THAT BEST MATCH THE MEAN-CORRECTED F_{11}/F_{12} AND [12]−[25] FOR EACH SE INDEX

SE	Mixture	τ_{10}	ΔR ($\times 10^{15}$ cm)	Δt (yr)
1.....	Alumina	0.7	1.7	55
2.....	Alumina	1.1	1.2	37
3.....	Alumina	1.5	1.0	33
3.....	Silicate	10.5	1.1	34
4.....	Silicate	7.4	2.0	34
5.....	Silicate	4.7	6.8	215
6.....	Silicate	3.3	14.8	470
7.....	Silicate	2.3	35.2	1120

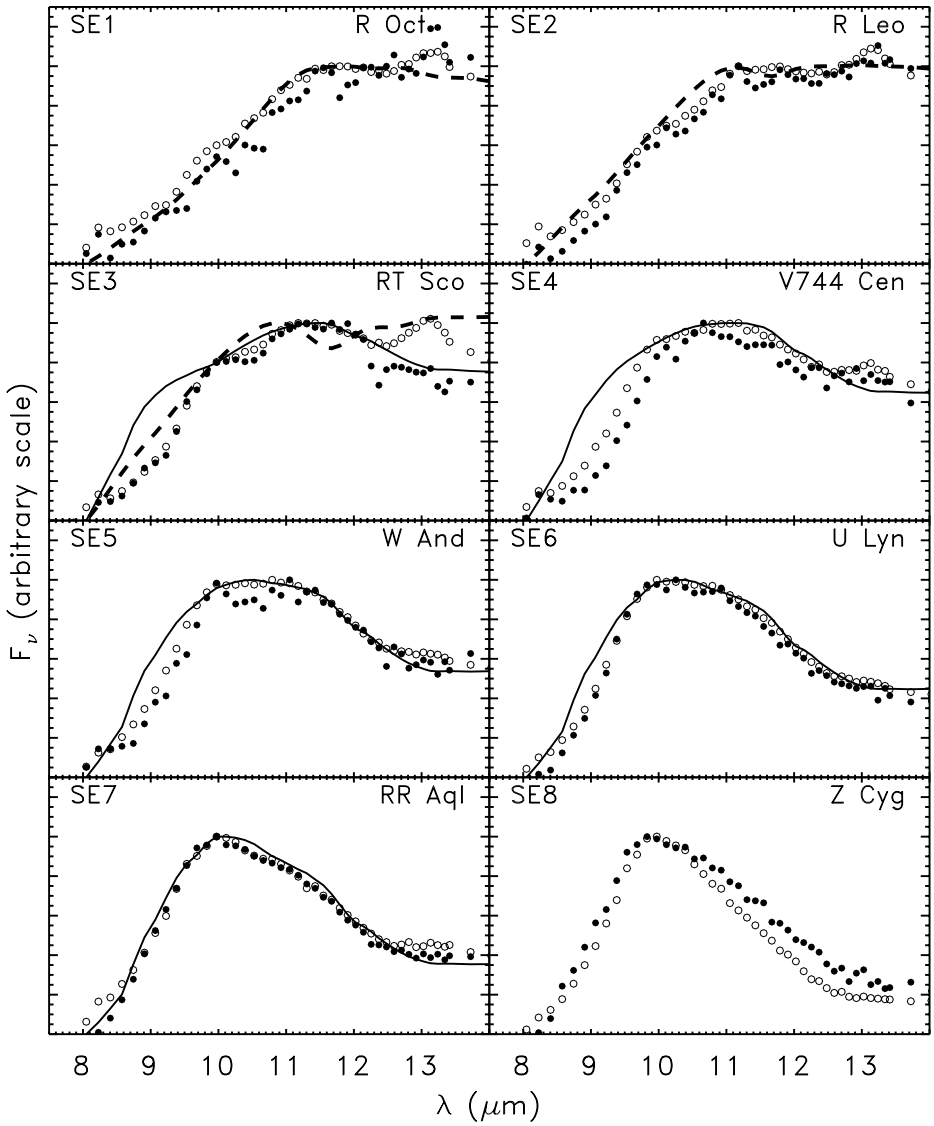

FIG. 10.—Comparison of dust spectra extracted from the models to spectra from actual LRS data. All data are shown after the stellar continuum has been subtracted. For each silicate emission index, the figure plots the dust spectrum extracted from a typical source (*filled circles*, named in the upper right-hand corner of each panel), the sum of all bright spectra of that SE index (*open circles*), and the best matching model (dashed line for alumina dust; solid line for silicates). The sums are produced by adding the continuum-subtracted dust spectra of the brightest sources for each index and dividing by the peak dust flux. The individual spectra are also normalized to their peak dust flux.

Normally, one expects optically thick shells, where dust emission dominates the SED, to produce very red [12]−[25] colors. However, if the dust is warm enough, it will produce a blue [12]−[25] color.

One issue in this wavelength range is the 13 μm feature, which does not arise from amorphous alumina dust or amorphous silicates and thus could not be produced by our models. Another issue with using these shells to fit the structured silicate emission is that the models produce too much flux in the vicinity of 9 μm.

4. DISCUSSION

Our radiative transfer models show that the upper silicate dust sequence (classic silicate emission) results from optically thin shells of amorphous silicate dust. The lower silicate dust sequence (broad, low-contrast emission) arises from optically and geometrically thin shells of alumina dust. Surprisingly, the structured silicate spectra that populate the central silicate dust sequence can arise from *optically thick* shells of amorphous silicates, but to match the [12]−[25] colors, the shells must be *geometrically thin.*

4.1. *Two Grain Chemistries*

Few astronomers will be surprised that amorphous silicate grains provide such a good fit to spectra on the upper silicate dust sequence. To fit the remainder of the sequence, a wide variety of dust components have been proposed, but the models here show that only the addition of alumina dust is needed.

Our results are similar to the recent work of Lorenz-Martins & Pompeia (2000), who also use combinations of alumina and silicate dust to fit the silicate dust sequence. We both agree about the two ends of the sequence, with alumina-dominated shells needed for the broad emission feature and silicate-dominated shells needed for the classic narrow feature, but they argue that nearly even mixtures of

alumina and silicates can fit the structured silicate spectra in the central sequence, while this study finds that the only acceptable dust mixtures are those where one of the two components dominates the other. In particular, they model five sources that they describe as intermediate. They fit RS Librae (an SE2; really a broad source) with a 53% silicate dust mixture, while three SE3 sources and one SE6 source require a mixture of approximately 60% silicates.

Lorenz-Martins & Pompeia (2000) used different dielectric constants for their alumina dust. They combined the 8–500 μm data for porous amorphous Al_2O_3 (Begemann et al. 1997) with the near-infrared data for the γ-Al_2O_3 *ISAS* sample from Koike et al. (1995). We used the latter sample at all wavelengths, and, as Figure 10 shows, it produces an excellent match to the SE1–SE2 spectra and a reasonable match to the SE3 spectrum. We have tested the combination of alumina constants used by Lorenz-Martins & Pompeia (2000) and find that the modified constants produce results similar to ours. The constants from Koike et al. fit the SE1–SE2 range better, but the Begemann constants allow higher percentages of alumina to silicates (up to 40%), and they can fit spectra one index further, up to SE4. Larger fractions of alumina do not work with either set of constants. Thus, we conclude that an oxygen-rich circumstellar shell will be dominated by either silicates or alumina.

4.2. *Shell Thickness and [12]−[25] Color*

IE95 used radiative transfer models of dust shells composed of pure amorphous silicates to argue that increasing the optical depth would shift a spectrum classified in the LML system as Sil++ to Sil+ and then Sil (i.e., SE3 through SE8, or *up* the silicate dust sequence). Model set 1, on the other hand, shows that increasing the opacity of the shell will broaden the silicate emission feature, shifting it *down* the silicate dust sequence, the direction *opposite* to the findings of IE95. This discrepancy results from a difference in constraints. Figures 4 and 5 in IE95 show that as they increase the opacity of the shell, the contrast of the shell compared to the star grows, and the [12]−[25] color of the system reddens.[4] IE95 classified their model spectra based on the contrast of the shell to the star and the infrared color of the system, but not the *shape* of the dust emission feature, which defines both the LML classes and the SP silicate emission indices.

Model set 1 revealed that increasing the optical depth of a dust shell while holding the inner and outer radii constant broadened the silicate emission feature while increasing the [12]−[25] color of the star-shell system. Broadening the emission feature will push a spectrum down the silicate dust sequence, but further down the sequence, the colors grow *bluer*, not redder. This effect is apparent when analyzing sources by LML class or even LRS characterization (see Tables 3 and 4, respectively, in Sloan & Price 1995).

Model set 2 showed that this discrepancy can be resolved by decreasing the geometric thickness of the shell as the opacity increases. Bringing the outer radius of the dust shell closer to the star increases the average temperature of the dust and produces bluer [12]−[25] colors. This leads us to believe that the [12]−[25] color is actually an indicator of the geometric thickness of the dust shell.

[4] IE95 described their results in terms of a "[25]−[12]" color; see the Appendix for an explanation of how this relates to the more commonly used [12]−[25] color.

While IE95 argue that circumstellar shells can be fully parameterized by the total shell opacity τ_F (given a grain composition and grain density distribution), Egan et al. (1996) and Ivezić & Elitzur (1997) have shown that the geometric thickness of the shell influences the shape of the SED in the mid- and far-infrared. Model set 2 demonstrates that for the classes SE6 through SE3, large geometric thicknesses produce [12]−[25] colors that are redder than any actually observed. Thus, the crucial parameter in matching the SEDs of oxygen-rich AGB stars over large wavelength ranges is the geometric thickness of the dust shell.

4.3. *Implications of Thin Shells*

If the dust shell has a finite geometric thickness, then it follows that the mass-loss rate must change with time. Table 3 includes a column headed "Δt," which gives the time needed to traverse ΔR at the assumed outflow velocity of 10 km s^{-1} for the model that best fits each SE index. These times are surprisingly short for the lower and central portions of the silicate dust sequence, ranging between 30 and 60 yr. On the upper sequence, these times increase to hundreds of years, up to 1100 yr.

High-resolution imaging has revealed concentric shells around several evolved sources. Crabtree, McLaren, & Christian (1992) imaged IRC +10216 optically and estimated that mass-loss outbursts lasting 200–400 yr each were responsible for the structure they observed. Optical images of NGC 7027 (Bond et al. 1997) reveal multiple shells spaced by intervals we estimate to be 200–500 yr. Sahai et al. (1998) measured the spacing between rings around AFGL 2688 (the Cygnus Egg) and estimate outburst periods of 75–200 yr and a total time of 150–450 yr from the start of one cycle to the next.

Closer in to the central source, spectroscopic and interferometric observations have also revealed multiple shells in both IRC +10216 and α Orionis. Sloan & Egan (1995) clearly resolved two shells around IRC +10216 using long-slit spectroscopy, and they show that radiative transfer models with two shells match both the SED and mid-infrared spectrum much better than single-shell models (they also list several earlier references observing the complicated shell structure around this well-studied source). Sloan & Egan (1995) suggest that the mass loss from IRC +10216 may have been interrupted during the period from 1900 to 1940.

Sloan, Grasdalen, & LeVan (1993) used long-slit spectroscopy to resolve two dust shells around α Ori, and their results are consistent with interferometric measurements by Bester et al. (1991). Both groups find that the outer shell has an approximate radius of 1″, and Danchi et al. (1994) suggest that it may result from a disturbance in the atmosphere of the central star in the mid 1920s. More recent mid-infrared spectroscopic monitoring (Bester et al. 1996; Monnier, Geballe, & Danchi 1998, 1999) suggests that α Ori might be in the midst of another mass-loss outburst, which would put the total cycle on an approximately 70 yr basis.

Clearly, the evidence for a time-variable mass-loss rate from evolved stars is strong. Not only is the case quite convincing, but the periodicity indicated by our models agrees well with the range of apparent periodicities.

Multiple shells could solve the difficulties fitting the [12]−[25] colors of the SE8 sources with optically and geometrically thin shells. As an example, assume that the current mass loss outburst has continued for 50 yr and that

the previous outburst ended 350 yr prior to the current episode. In this case, the outer shell would have an inner radius of $340R_*$. For optically thin cases, $T \propto r^{-1/2}$, and at R_{in}, the remnant shell would have a temperature of 135 K, which implies peak dust emission at 21 μm. Dust at this temperature would radiate more strongly in the 25 μm band than in the 12 μm band and would redden an SE8 model sufficiently to agree with the observed colors.

5. CONCLUSION

We have used radiative transfer models to study the effects of grain chemistry, optical depths, dust formation radius, and shell thickness on the spectral emission from circumstellar shells. We have constrained these parameters by fitting the flux ratios F_{10}/F_{11} and F_{10}/F_{12} (as defined by SP), the [12]−[25] color, and the dust spectrum as observed by the LRS aboard *IRAS*.

This study of alumina and amorphous silicates reveals that both are needed to fit the wide range of observed spectral shapes, but a given dust shell will be dominated by one component or the other. Relatively even mixtures of the two do not fit the observed data. Other dust compositions are not necessary.

Spectra showing the classic narrow 10 μm emission feature arise from optically thin shells dominated by amorphous silicates. Spectra with broad low-contrast emission peaking $\sim$11–12 μm arise from optically and geometrically thin shells composed primarily of alumina dust. The former populate the upper silicate dust sequence, while the latter dominate the lower.

Amorphous silicate shells can also fit the central region of the silicate dust sequence (sometimes described as structured silicate spectra), but the shells must be simultaneously optically thick and geometrically thin. These models work quite well, as Figures 8, 9, and 10 show. The high opacity is needed to move the spectrum down the silicate dust sequence, and in order to match the observed [12]−[25] colors, the outer radius of the shell cannot be too large compared to the inner radius. This result implies that the mass-loss process must be periodically interrupted.

This research made use of the LRS database maintained at the University of Calgary, the SIMBAD database at Strasbourg, and data and software distributed by the NASA Astronomical Data Center. G. C. S. received support from the Phillips Lab Scholar program, the National Research Council, and the National Science Foundation (grant INT-9703665) during the various phases of this project. He would also like to thank the Division of Physics at the University of New England in Australia, the School of Physics at the Australian Defence Force Academy, and the Department of Physics at Virginia Tech for hosting him while this work was underway.

APPENDIX A

In this paper, we have followed standard photometric definitions when defining the [12]−[25] colors. Using the zero-magnitude fluxes for the non–color-corrected 12 and 25 μm *IRAS* filters determined by Cohen et al. (1992), the magnitudes and colors are defined as:

$$[12] = -2.5 \log \left(\frac{F_{\nu(12)}}{40.14 \text{ Jy}} \right),$$

$$[25] = -2.5 \log \left(\frac{F_{\nu(25)}}{9.49 \text{ Jy}} \right),$$

$$[12] - [25] = 2.5 \log \left(\frac{F_{\nu(25)}}{F_{\nu(12)}} \right) + 1.60 . \quad \text{(A1)}$$

The zero-magnitude fluxes as originally defined in the *IRAS* Explanatory Supplement (Beichman et al. 1986) were 28.3 Jy at 12 μm and 6.73 Jy at 25 μm, which resulted in an additive constant for [12]−[25] of 1.56, slightly different from 1.60 used here.

IE95 define a color without using the zero-magnitude fluxes or the scaling factor of −2.5, giving

$$([\lambda_a] - [\lambda_b])_{\text{IE95}} = \log \left[\frac{F_\nu(\lambda_a)}{F_\nu(\lambda_b)} \right], \quad \text{(A2)}$$

so

$$[12] - [25] = 2.5([25] - [12])_{\text{IE95}} + 1.60 . \quad \text{(A3)}$$

Thus, while the zero points and scales differ, both measures increase in the same sense; that is, the more positive the quantity is, the redder the color. By the definition of IE95, a 10^4 K blackbody has a $([25]-[12])_{\text{IE95}}$ color of −0.40, while in a Vega-based system (or more precisely, a system based on a Kurucz model of α Lyrae; Kurucz 1979) such a blackbody has a color of approximately 0.0 at all wavelengths.

REFERENCES

Begemann, B., Dorschner, J., Henning, T., Mutschke, H., Guertler, J., Koempe, C., & Nass, R. 1997, ApJ, 476, 199
Beichman, C. A., Neugebauer, G., Habing, H. J., Clegg, P. E., & Chester, T. J. 1986, *IRAS* Explanatory Supplement (Washington, DC: NASA)
Bester, M., Danchi, W. C., Degiacomi, C. G., Townes, C. H., & Geballe, T. R. 1991, ApJ, 367, L27
Bester, M., Danchi, W. C., Hale, D., Townes, C. H., Degiacomi, C. G., Mekarnia, D., & Geballe, T. R. 1996, ApJ, 463, 336
Bond, H. E., Fullton, L. K., Schaefer, K. G., Ciardullo, R., & Sipior, M. 1997, in IAU Symp. 180, Planetary Nebulae, ed. H. J. Habing & H. J. G. L. M. Lamers (Dordrecht: Kluwer), 211
Chan, S. J., & Kwok, S. 1990, A&A, 237, 354

Cohen, M., Walker, R. G., Barlow, M. J., & Deacon, J. R. 1992, AJ, 104, 1650
Crabtree, D. R., McLaren, R. A., & Christian, C. A. 1987, in Late Stages of Stellar Evolution, ed. S. Kwok & S. R. Pottasch (Dordrecht: Reidel), 145
Danchi, W. C., Bester, M., Degiacomi, C. G., Greenhill, L. J., & Townes, C. H. 1994, AJ, 107, 1469
Egan, M. P., Kwok, S., Leung, C. M., & Price, S. D. 1996, A&A, 308, 738
Egan, M. P., & Leung, C. M. 1995, ApJ, 444, 251
Egan, M. P., Leung, C. M., & Spagna, G. F. 1988, Comput. Phys. Commun., 48, 271
Engelke, C. W. 1992, AJ, 104, 1248
Fogel, M. E., & Leung, C. M. 1998, ApJ, 501, 175
Hron, J., Aringer, B., & Kerschbaum, F. 1997, A&A, 322, 280
IRAS Science Team 1986, A&AS, 65, 607
Ivezić, Ž., & Elitzur, M. 1995, ApJ, 445, 415 (IE95)
———. 1997, MNRAS, 287, 799
Koike, C., Kaito, C., Yamamoto, T., Shibai, H., Kimura, S., & Suto, H. 1995, Icarus, 114, 203
Kurucz, R. L. 1979, ApJS, 40, 1
Leung, C. M. 1976, J. Quant. Spectrosc. Radiat. Transfer, 16, 599
Little-Marenin, I. R., & Little, S. J. 1988, ApJ, 333, 305
———. 1990, AJ, 99, 1173
Little-Marenin, I. R., & Price, S. D. 1986, in Summer School on Interstellar Processes, ed. D. J. Hollenbach & H. A. Thronson. Jr. (NASA Tech. Memo. 88342; Moffet Field: NASA/ARC), 137
Lorenz-Martins, S., & Pompeia, L. 2000, MNRAS, 315, 856
Monnier, J. D., Geballe, T. R., & Danchi, W. D. 1998, ApJ, 502, 833
———. 1999, ApJ, 521, 261
Onaka, T., de Jong, T., & Willems, F. J. 1989, A&A, 218, 169
Ossenkopf, V., Henning, T., & Mathis, J. S. 1992, A&A, 261, 567
Sahai, R., et al. 1998, ApJ, 493, 301
Sloan, G. C., & Egan, M. P. 1995, ApJ, 444, 452
Sloan, G. C., Grasdalen, G. L., & LeVan, P. D. 1993, ApJ, 404, 328
Sloan, G. C., & Price, S. D. 1995, ApJ, 451, 758
———. 1998, ApJS, 119, 141
Vardya, M., de Jong, T., & Willems, F. 1986, ApJ, 304, L29